A novel experimental setup for in-situ optical and X-ray imaging of laser sintering of polymer particles

Prakhyat Hejmady,[1,2] Lucien C. Cleven,[1] Lambèrt C. A. van Breemen,[1] Patrick D. Anderson,[1] and Ruth Cardinaels[1, a)]

[1)]*Polymer Technology, Department of Mechanical Engineering, Eindhoven University of Technology, P.B. 513, 5600 MB Eindhoven, The Netherlands*

[2)]*Brightlands Materials Center, 6167 RD, Geleen, The Netherlands*

We present a unique laser sintering setup that allows real time studies of the structural evolution during laser sintering of polymer particles. The device incorporates the main features of classical selective laser sintering (SLS) machines for 3D printing of polymers, and at the same time allows in-situ visualization of the sintering dynamics with optical microscopy as well as X-ray scattering. A main feature of the setup is the fact that it provides local access to one particle-particle bridge during sintering. In addition, due to the small scale of the device and the specific laser arrangement process parameters such as temperature, laser energy, laser pulse duration and spot size can be precisely controlled. The sample chamber provides heating up to 360 ºC, which allows for sintering of commodity as well as high performance polymers. The latter parameters are controlled by the use of a visible light laser combined with an acousto-optic modulator for pulsing, which allows small and precise spot sizes and pulse times and pulse energies as low as 500 μs and 17 μJ. The macrostructural evolution of the particle bridge during sintering is followed via optical imaging at high speed and resolution. Placing the setup in a high flux synchrotron radiation with a fast detector, simultaneously allows in-situ time-resolved X-ray characterizations. To demonstrate the capabilities of the device, we studied the laser sintering of two spherical PA12 particles. The setup provides crucial real-time information concerning the sintering dynamics as well as crystallization kinetics, which was not accessible up to now.

a)R.M.Cardinaels@tue.nl

I. INTRODUCTION

Laser sintering (LS) of polymer powders, also known by its trade name selective laser sintering (SLS), is an emerging 3D printing technology, by which complex parts are manufactured layer-by-layer[1–5]. In SLS, polyamide 12 (PA12) is the most commonly used polymer due to their large sintering window[6]. Though this technique receives significant interest from industry as well as academia[7–9], the final products often suffer from poor mechanical properties. Due to limited control over the process parameters as well as incomplete insights in the relations between process conditions and structure development during laser sintering, the final products cannot be produced with tailored and reproducible structural/mechanical properties[10]. Moreover, porosity, poor layer-to-layer adhesion and dimensional inaccuracy are some of the commonly found defects in such SLS printed parts[11]. While there are ample studies showing the effects of laser sintering on the microstructure, crystalline morphology and mechanical properties of polymers, they are all limited to post-mortem characterization techniques thus lacking information on the actual structure development[12,13]. Since shape evolution and crystallization kinetics during laser sintering are complex and coupled processes involving non-isothermal, non-homogeneous temperature profiles and complex flow fields, studies with high temporal and spatial resolution are required to provide fundamental insights in the effects of processing conditions on the microstructure development during laser sintering.

Hot stage microscopy has been a convenient technique to observe coalescence of two polymer particles[14] during and after heating, and to validate analytical models describing sintering dynamics[15–17]. Although this technique is suitable to study traditional polymer processing operations such as rotational moulding, it misses several aspects typical for laser sintering. In laser sintering, the laser pulse causes fast heating followed by cooling, the speed of which is essential for the sintering kinetics[18] but also for the melting and crystallization of the polymer. In addition, the heat distribution in the particles due to the laser is not uniform, which can lead to partial melting and further affects the flow, and therefore the structure development within the particles[19]. To investigate polymer structure, X-ray diffraction is a powerful and widely used technique[20]. Ex-situ X-ray diffraction and scattering experiments have been utilized to study the crystalline microstructure within SLS printed parts[21], but studies on time dependent microstructure developments that take place during the process are not available. For traditional polymer processing operations such as extrusion or injection moulding, custom-designed setups have been

developed that can incorporate high flux synchrotron radiation to allow for in-situ time resolved X-ray studies of polymer crystalline morphology development[22–24]. Moreover, for extrusion additive manufacturing it was recently shown that in-situ characterization of the extruded material via infrared thermography and Raman spectroscopy can provide valuable information about the weld formation and crystallization kinetics during extrusion additive manufacturing.[25,26] Recently, laser sintering of metals has been studied in-situ and time-resolved by means of X-rays[27,28], but these studies were concentrated on using X-ray attenuation to study powder motion, melting and melt dynamics in a bed of metal powder. Zhao et al. used time-resolved X-ray diffraction to study the kinetics of the phase transformations of α-β Titanium Alloy (Ti-Al-4v) upon solidification, using a spot size around five times bigger than the particle size and targeting a metal powder bed[29]. However, up to now, experimental setups allowing to provide real time information on the melting dynamics and crystallization kinetics during sintering of polymers as well as setups targeting single particle pairs are not available. Intrinsically transient processes like laser sintering pose many challenges in building such a system, which should incorporate the main features of an SLS machine and at the same time should allow optical visualization and X-ray scattering/diffraction characterization. Recently, we have developed a setup that allows optical visualization of laser sintering and have studied laser sintering of amorphous polystyrene[30]. In the present work, we present an experimental setup that not only enables us to study laser sintering of polymer particle doublets with precisely controlled sintering parameters, but also enables in-situ X-ray characterization thereby providing access to the polymer internal microstructure development during sintering.

II. DESIGN AND DESCRIPTION

The key feature of the experimental setup is the ability to precisely control the laser impact energy at the interface of two polymer particles while simultaneously visualizing the sintering process optically and performing in-situ X-ray experiments. This gives us the exclusive advantage to be able to track the dynamics and kinetics of macro- and microstructure development during the sintering process, which is not possible in commercial SLS machines. Fig. 1 shows the layout of the experimental setup as arranged in the beamline. The polymer particle pair to be sintered is placed in the sample chamber, which allows for X-ray access via the side windows and optical

visualization as well as laser entrance from the top. The main components of the setup namely the laser, the sample chamber and the imaging system are discussed in more detail in the following sections.

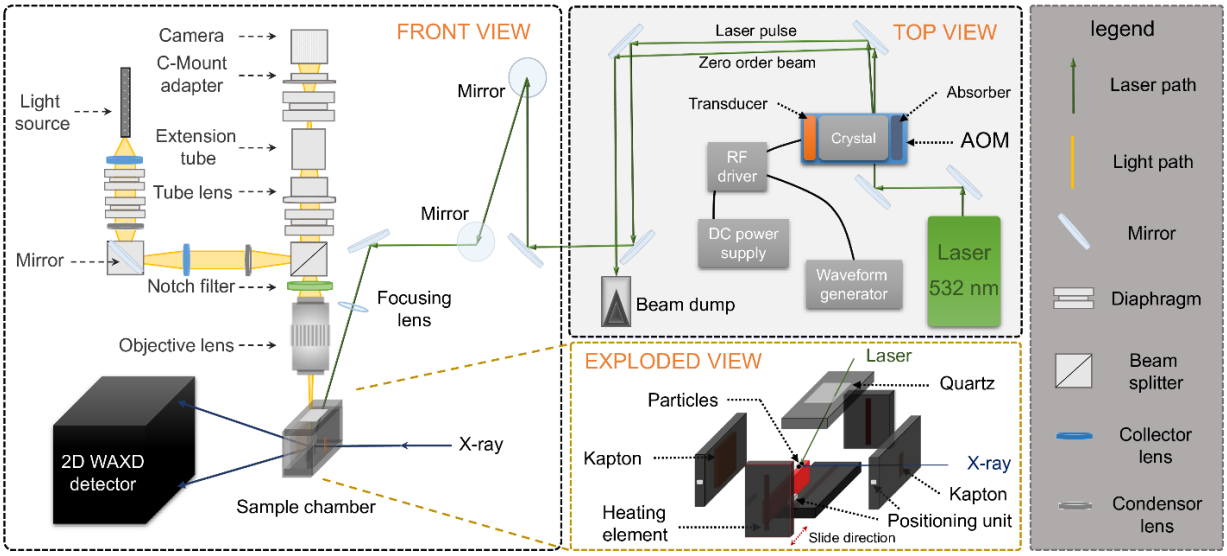

FIG. 1. Schematic representation of the experimental setup with in-situ X-ray scattering/diffraction capability. Front and top view represent the visualization and laser systems respectively, which were arranged on a 600 mm x 600 mm optical table. The exploded view of the sample chamber shows the particle substrate.

A. Laser

A visible-light laser is used, as this allows a more precise control over the laser power and facilitates lower power values as compared to CO_2 lasers, which are used in classical SLS machines. In addition, the smaller wavelength enables smaller laser spot sizes. High power stability, low beam divergence and a high quality factor M^2 are essential to be able to focus the laser beam to the desired spot size and to ensure precise control over the laser impact energy. In our setup, we use a Genesis MX STM from Coherent, which is a continuous wave (CW) laser of 532 nm wavelength with a spatial TEM00 mode, which provides a Gaussian intensity distribution. The beam waist diameter is 2 mm with a beam divergence of < 0.7 mrad and a beam quality factor, $M^2 < 1.1$. The output power ranges between 0.02 mW and 2 W with a beam stability within 2%. Diverting the laser through the objective lens used for visualization limits the final spot size achievable. Furthermore the peak intensities of the laser pulse exceed the damage threshold limit

of the infinity corrected objective. Hence, the laser is sent directly next to the objective lens under the minimum possible incidence angle with respect to the objective lens (30º). By using focusing lenses with different focal lengths, the final spot size of the laser beam can be varied as[31]:

$$D_s = \frac{1.27 \cdot M^2 \cdot \lambda \cdot f}{D_l} \quad (1)$$

where M^2 is the laser beam quality factor, λ the wavelength, f the focal length of the lens and D_l the beam waist diameter of the laser. For in-situ experiments we use a focusing lens with a focal length of 100 mm. By tight focusing we achieve a final spot diameter of 40 μm, whose size was verified by optical imaging and corresponds to the value predicted by Eqn. 1. To simulate the limited laser-impact time on the sample during actual SLS processes due to the fast movement of the laser over the powder bed, the laser is pulsed with a well-defined pulse length as well as pulse energy. To do so, the beam path of the continuous wave laser is diverted using mirrors (Altechna HR laser line mirror, reflectivity: 99.5%), through an acousto-optic modulator (AOM) from Isomet, which has an aperture of 2 mm and maximum modulation frequency of 30 MHz. In single pulse-mode, pulses as short as 500 μs can be sent with a minimum rise and fall time of 360 ns. AOM's are primarily used to control laser beam intensity, and their main components are a piezoelectric transducer, a crystal and an absorber. By switching on and off the modulation within the AOM, the output intensity can be controlled by redirecting part of the laser beam to a beam dump. To generate the modulation signal, the AOM is connected to an RF driver (Isomet) which in-turn is connected to a DC power source (Basetech) and waveform generator (Keysight 33500B). Via the waveform generator and RF driver, any arbitrary waveform can be supplied to the piezoelectric transducer, which generates an acoustic wave in the crystal. The absorber damps the RF signal such that secondary waves due to reflection are suppressed. Due to the photo-elastic effect, areas of compression and densification are created in the crystal bulk, which provides a single pulsed first order beam under an angle of 0.7º with respect to the zeroth order continuous wave beam. The former is then diverted to the sample chamber and the later to the beam dump, as schematically shown in Fig. 1. With a known laser output power, which is measured using a Gentec XLP12 thermopile, and a known waveform signal supplied, single pulses with energy values ranging from a minimum of 17 μJ/pulse upto a maximum of 0.5 J/pulse can be sent. The laser pulse energy is measured using a Gentec QE12, which is a pyroelectric based energy meter with a precision of 0.5 μJ.

B. Sample Chamber

Another important feature of the setup is the heating chamber with a sample substrate which has been designed to meet the requirements on temperature accuracy and homogeneity. Furthermore, it allows to perform in-situ optical and X-ray measurements. The sample substrate (1 mm thickness) consists of mirror polished steel (roughness of 100 nm) to eliminate spurious reflections in the optical images. Furthermore, its width along the X-ray direction is minimized to avoid interference with the incoming or outgoing scattered X-ray beam. To facilitate the placement of the sample, the substrate is connected to one of the sides of the sample chamber which can be opened and closed by means of the rail slider and positioning units, as illustrated in Fig. 1. The sample chamber (32 mm x 70 mm x 32 mm) has a 3 mm thick quartz window (17 mm x 13 mm) on top that allows entering of the laser beam and optical visualization via an objective lens. Moreover, two side walls contain 0.025 mm thick Kapton windows to allow for entrance (2 mm x 10 mm) and exit (15 mm x 15 mm) of X-rays (Fig. 1). The sample to window distance on the scattering side was taken as small as possible (0.8mm), thereby facilitating 2θ scattering angles up to 45º, which is large enough to capture the main crystallization peaks of all common polymers. The chamber is built from aluminum with a wall thickness of 6 mm. An enclosure of low thermal conductivity (0.4 W/(m·K) at 400 ºC) around the box minimizes heat loss to the environment. Based on a heat analysis of the sample chamber including conduction and free convection to the environment at 25 ºC a heat loss of 17.9 W was estimated at a sample chamber temperature of 360 ºC. For heating, the side walls of the chamber as well as the bottom plate contain heating rods (three rods with length 60 mm and diameter 6 mm, 100 W) which provide sufficient heating power. In addition, K-type thermocouples (RS Pro, ±1 ºC accuracy) are integrated in the sample chamber to measure substrate and air temperature. Heating rods and thermocouples are connected to a temperature control unit (Hasco), which allows to regulate the temperature of the substrate and the air independently. Simultaneously, air and substrate temperature are monitored using calibrated voltcraft thermometer with K-type thermocouple. This allows to maintain the sample temperature within ± 0.6 ºC up to the maximum operating temperature of 360 ºC. These specifications ensure that common polyolefins as well as engineering plastics such as PEEK can be sintered within the heating chamber. Based on the thermal mass of the sample chamber, a maximum heating rate of 25 ºC/min can be obtained with the heating rods. Temperature overshoots from the desired set-point are avoided using PID control (Eurotherm).

C. Optical imaging system

Given the thin interface between the two polymer particles at the initial stages of sintering and the large curvature effects that dominate the coalescence process during sintering, the imaging system needs to provide adequate resolution. However, due to the high temperature of the sample chamber heat loss from the sample chamber can heat up and expand the lenses within the objective lens (maximum working temperature of 65 ºC) which can cause optical aberrations. This limits the usage of objective lenses with a high numerical aperture or low working distance. Moreover, sintering is a fast dynamic process, requiring minimum image acquisition times on the order of 50 ms, depending on the polymer type used. In order to fulfill these requirements and maintain geometrical flexibility for placement in the beamline, we custom designed the optical train for imaging. Fig. 1 illustrates the individual components of the optical train which mimics the architecture inside a microscope. The main components of the optical train are an infinity corrected Mitutoyo 20x objective lens (NA 0.28, working distance 30 mm) and a Pixelink (PL-D725MU-T) CMOS camera with 1 inch sensor size (2592 x 2048 pixels), which can capture images at 75 frames per second in full resolution. By reducing the region of interest, frame rates can be further increased. The objective lens is corrected for aberrations with a glass sample cover with a thickness of 3 mm, which corresponds to the thickness of the quartz glass in the sample chamber. This combination of high camera resolution and objective lens allows to capture images with 4.3 pixels/µm, which suffices for the length scales we are interested in. Moreover, no image distortions are observed while imaging at 360 ºC sample chamber temperature. Besides the main components, the optical train contains several auxiliary components. Right above the objective a notch filter (center wavelength 532±2 nm, Thorlabs) is placed to exclude reflected laser light from the optical train, which would otherwise lead to overexposure of the camera and hamper imaging. The tube lens used to focus the image on the camera is a bi-convex lens with a focal length of 200 mm, which equals the focal length of a Mitutoyo tube lens. This lens is placed in a zoom housing which provides a vertical translation of 4 mm with a precision of 0.5 mm per revolution, allowing to optimize image focusing. A 50:50 beam splitter is positioned between the tube lens and the objective lens which facilitates simultaneous illumination and imaging through the objective. Illumination is provided by a 150 W halogen light source (Intralux 6000) with intensity control knob, through a flexible optic cable. The cable is connected to the tube with two diaphragms as well as two collector and two condenser lenses to provide sufficient light intensity. A mirror at 45º

diverts the collimated light source into the beam splitter. In addition to this, the main body of the imaging system (above the tube lens) consists of two diaphragms which reduce internal reflections within the tubing which would otherwise cause image distortions. Furthermore, a tube system is placed to position the camera at a suitable distance of the bi-convex lens considering its focal length. The imaging setup is attached to a micromanipulator with a lateral resolution of 0.25 mm per revolution, for fine adjustments along the vertical direction.

D. Placement in the beamline

The complete setup, as schematically depicted in Fig. 1, is placed in the BM26 (DUBBLE) beamline at ESRF, in Grenoble (France) to perform wide-angle X-ray diffraction experiments[32]. Fig. 2 shows the setup mounted in the beamline, with the main components indicated. An imaginary laser path (green line) is indicated as a guide to the eye. The sample chamber is mounted on a PI M-111 x-y-z micromanipulator stage with 1 μm minimal incremental steps and 15 mm travel range, along all directions. This allows alignment with respect to the incoming X-ray beam. The inset picture in Fig. 2 shows a close-up of the sample chamber with the laser and X-ray paths indicated. To achieve a high signal to noise ratio, a metallic cone under vacuum is attached in front of the detector, such that the scattering from the air can be reduced. A synchrotron beam of 100 μm x 100 μm was achieved on the sample interface, using a JJ X-ray slit system. This beam size reduction method is the best compromise between maintaining sufficient intensity and focusing on the main sintering area. The wavelength of the X-rays was 0.9799 Å and the sample to detector distance was 409 mm. The sample-detector distance and tilt angle were calibrated using AgBe (silver behenate) for the WAXD experiments. We used a Pilatus 300K detector with a pixel size of 172 μm x 172 μm. Thereby a minimum exposure time of 0.3 s could be achieved. Considering the typical crystallization times, this acquisition time provides an optimal balance between signal-to-noise ratio and time resolution. This setup provided access to scattering vectors q up to 23 nm^{-1}, which corresponds to characteristic length scales ranging down to 0.28 nm. The Fit2D software[33] developed by the European Synchrotron Radiation Facility was used to analyze the 2D WAXD data. The acquired images were corrected for background noise and the beamstop as well as traces of the direct beam were masked.

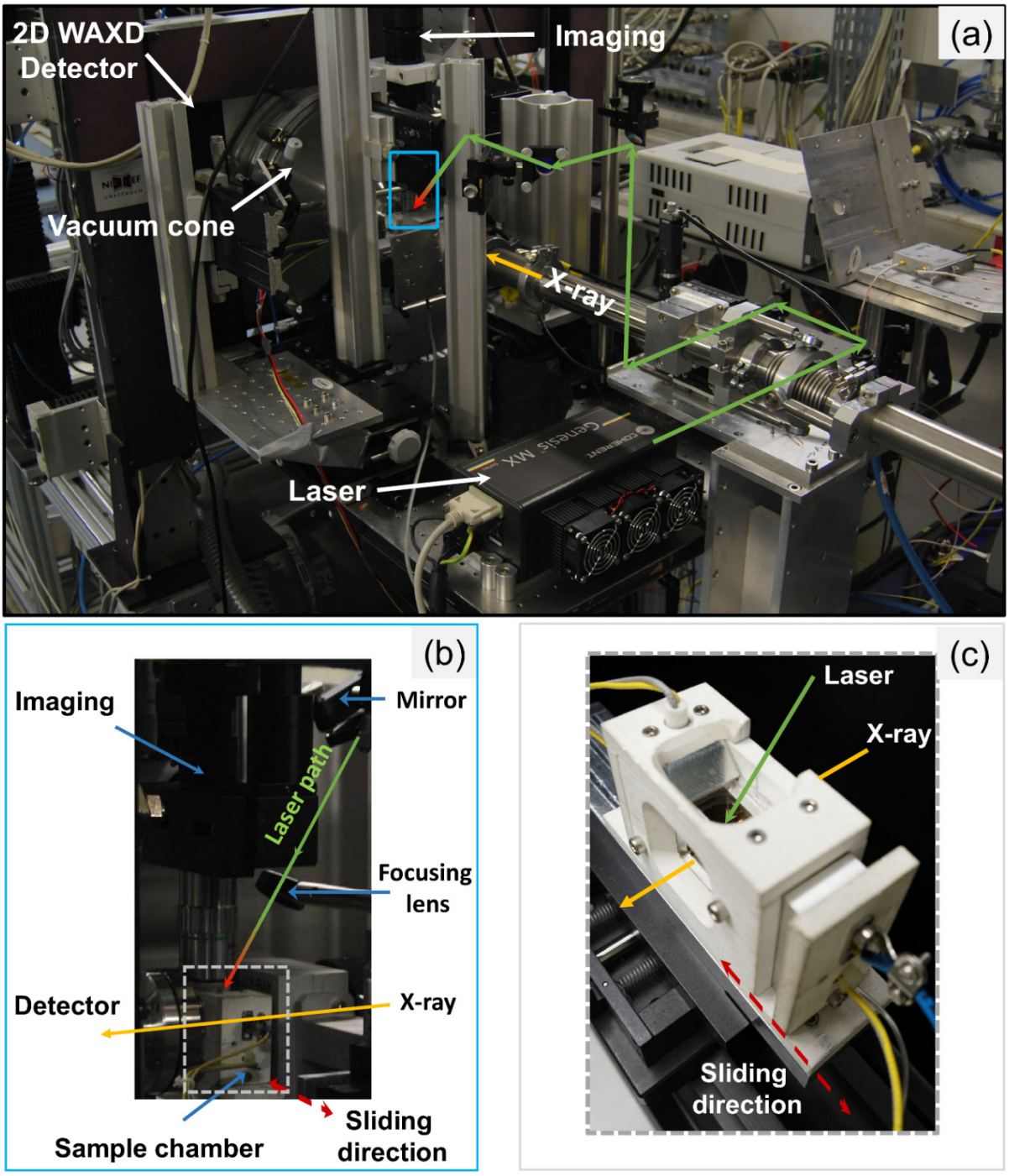

FIG. 2. Photograph of the experimental setup installed in the BM26 beamline at ESRF. (a) The setup is mounted on an x-y-z translator for positioning relative to the 2D WAXD detector and incident X-ray beam. (b) Inset picture shows the sample chamber with objective lens and vacuum cone. (c) Sample chamber.

III. EXPERIMENTAL PROCEDURE

A. Material

In our experiments we use spherical particles prepared from PA12 (Vestamide L-1700), which is free of flow and other additives. Before particle preparation, Nubian black dye (2 wt%) was added to the PA12 via solution mixing in benzylalcohol at 120 ºC. Addition of dye resulted in an absorption of 91% for visible light at 532 nm and a sample thickness of 100 μm. This enables the laser to locally heat up the sample and cause melting of the polymer particles allowing laser sintering. This PA12 with dye has a peak melting temperature T_m of 178 ºC and melting enthalpy of 56.4 J/g (as determined by differential scanning calorimetry at 5 ºC/min). To determine the half-time of crystallization ($t_{1/2}$), a specific thermal protocol was utilized by means of differential fast scanning calorimetry (FDSC)[34]. From the endothermic peak of melting after crystallization for varying isothermal times, the normalized enthalpy of fusion is plotted as a function of annealing time[34,35]. For PA12 with dye at 155 ◦C, the $t_{1/2}$ is evaluated to be 19.5 s.

Viscosity plays an important role in the sintering dynamics. The zero-shear viscosity, η_o is used as the main rheological parameter to determine the temperature-dependent flow behavior. To determine η_o, rheological measurements were performed on a stress-controlled rotational rheometer (MCR502 from Anton Paar) with a plate-plate geometry (diameter 25 mm). Measurements were carried out in the linear viscoelastic regime, which was determined by a strain sweep test (at 1 Hz). At sufficiently high temperatures above the glass transition and melt temperature of the polymer, the viscosity of most polymers is known to show an Arrhenius dependency with respect to temperature, given by[36]:

$$\eta = \eta_{\mathrm{ref}} \left[\frac{E_a}{R \cdot T}\right] \qquad (2)$$

where η is the viscosity, E_a the activation energy, R the universal gas constant, T the temperature and η_{ref} the pre-exponential factor.

Fig. 3 shows the zero-shear viscosity data of PA12 with 2 wt% black dye at four different temperatures fitted with the Arrhenius equation. An activation energy E_a = 32.5 kJ/mol was obtained, which is close to literature values for PA12, despite the difference in molecular weight[37]. The viscosity at 210 ºC is 125 Pa·s. The surface tension Γ, of PA12, which is relevant for the sintering process, is equal to 34.3 mN/m[38]. Finally, the thermal conductivity k is 0.12 W/(m·K)[39] and the heat capacity c_p is 1200 J/(kg·k), as determined from DSC measurements.

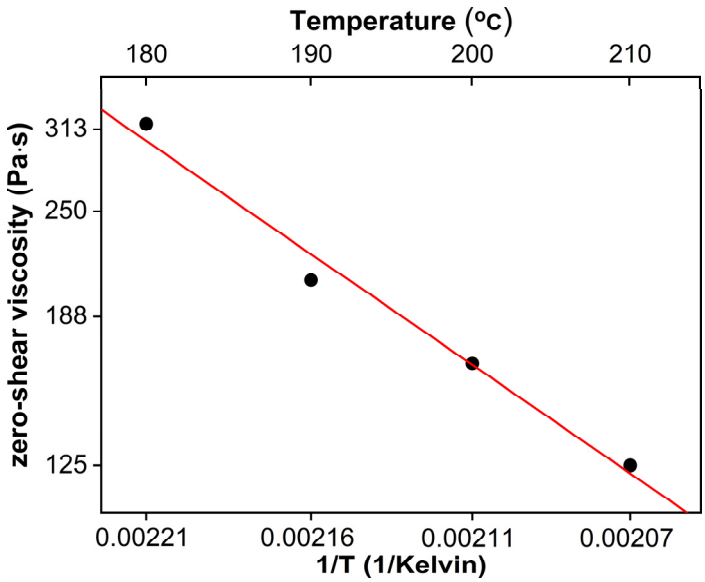

FIG. 3. Arrhenius plot for zero-shear viscosity versus temperature. Symbols are experimental data, line is a fit with Eq. (2).

B. Micromanipulation of polymer particles

To perform sintering experiments, two polymer particles of the same size placed adjacent to each other, with their interfaces being in contact, are required. For this, it is important to be able to manipulate polymer particles irrespective of their size and polymer type. We have developed a manipulation technique that allows to pick and place such polymer particles, in a non-destructive manner. Thereto, the sample substrate from the sample chamber is placed in a home-built particle manipulation setup, as shown in Fig. 4. The main components are a horizontal optical train and a manipulation probe connected to a voltage source. Each component is mounted on an x-y-z manipulator, and can thus be positioned individually. The imaging system is similar to the one described in Section 3.C. The illumination mode in this case is transmission, with a halogen source of 150 W power. The DC voltage source can generate voltages between 0.5 V and 90 V and its outputs are connected to a tungsten probe with a tip diameter of about 25 μm as well as to the substrate.

The particle manipulation procedure is demonstrated in Fig. 5, where PA12 particles of 115 μm radius are manipulated before performing in-situ measurements. First, similarly sized particles are deposited on the mirror polished stainless steel substrate on random locations. Then the imaging system and light source are positioned in line with a particle on the substrate. The tungsten probe is then positioned within the field of view of the camera. Subsequently, a

positive and negative voltage is applied to the probe and the substrate, respectively.

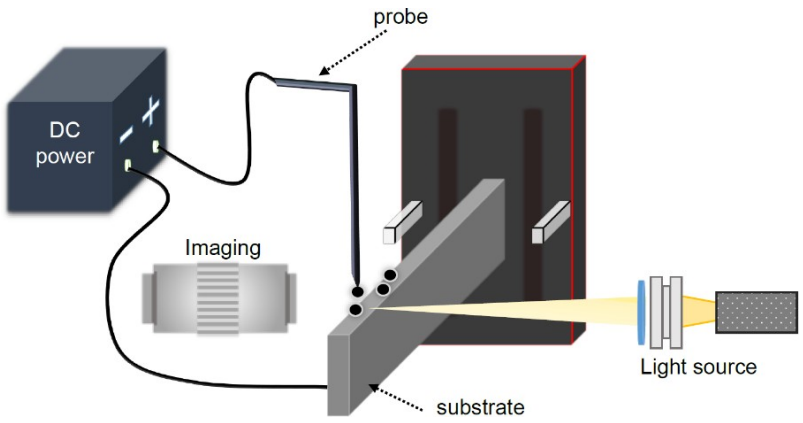

FIG. 4. Schematic representation of the particle manipulation setup. Each component is mounted on an x-y-z translator base, which allows to position them independently.

By applying a voltage to the probe and substrate, a non-uniform electrostatic field between both is generated. When a polymer particle is present within such an electric field, a dielectrophoresis force is exerted on it[40], which in this case leads to attraction towards the tungsten probe. By translating the substrate a similar-sized particle can be found, keeping the probe with particle within focus. Once the second particle is also in focus, the probe is positioned close to the second particle. By switching off the voltage, the first particle drops from the probe onto the substrate next to the second particle. While positioning the particles, care is taken to align the particle pair perpendicular to the horizontal optical train and X-ray beam, by ensuring that the particle edges of both particles are in focus (last image in Fig. 5). Once both particles are positioned, the substrate is carefully placed back into the sample chamber.

C. Micropositioning of a particle for in-situ X-ray characterization

To study the crystallization kinetics of the molten polymer in the sintered bridge, it is important that the interface between both particles is in-line with the X-ray source and detector. A coarse X-ray scan, performed by translating the sample chamber, along x- and z-direction enables to determine the location of the particles from the intensity value of the photodiode aligned with the X-ray source.

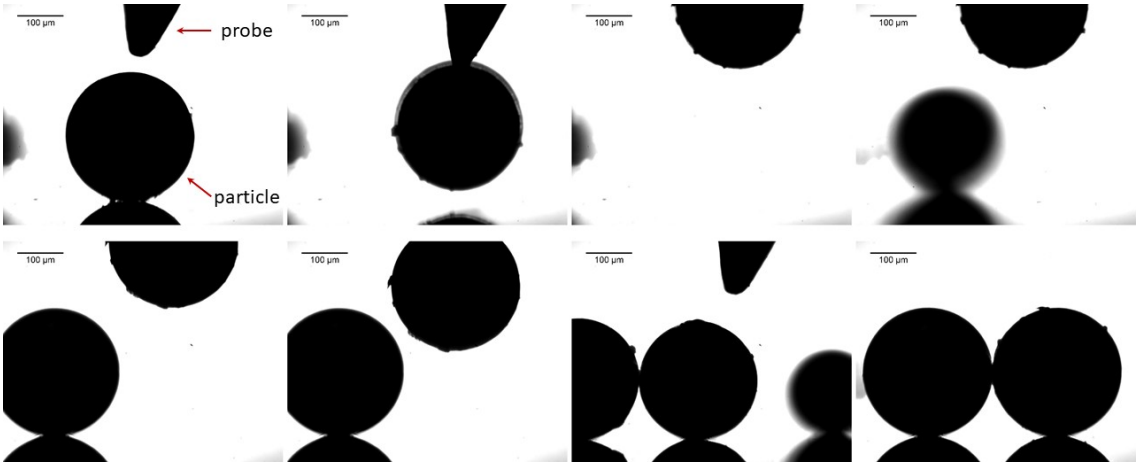

FIG. 5. Image sequence (from top left to bottom right) shows a non-destructive way of manipulating PA12 particles of 115 μm radius by applying a voltage between the probe and the substrate.

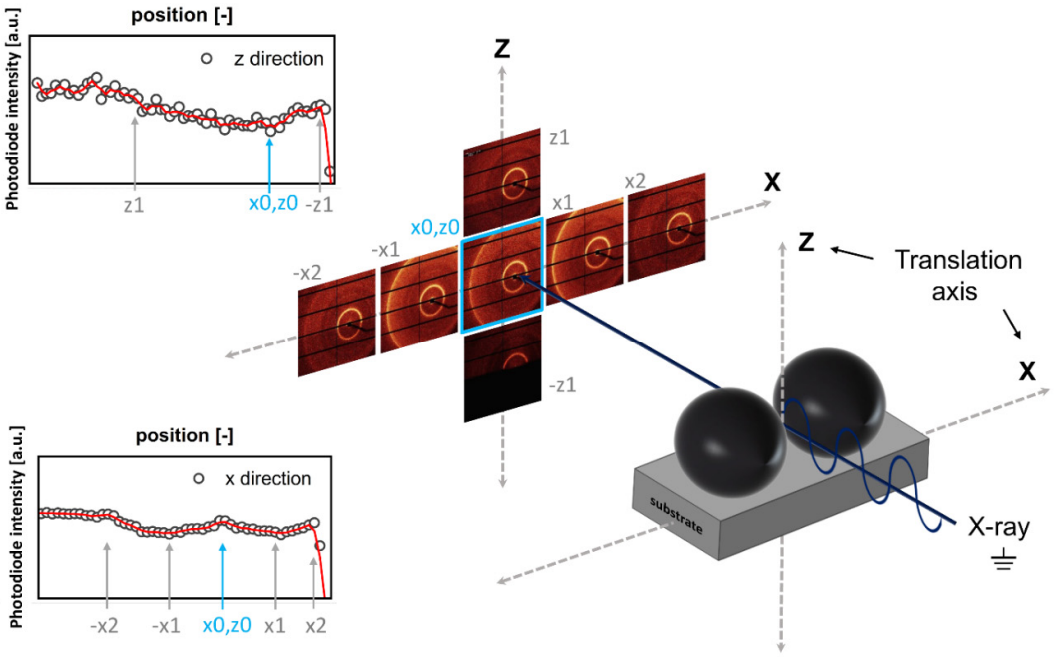

FIG. 6. Illustration of the X-ray scanning technique to find the interface between the particles. The X-ray beam and detector are stationary. By translating the substrate in x and z direction, different X-ray patterns are obtained (indicated by x,z coordinates of the substrate). The substrate obstructs the X-ray beam whereas the presence of a particle maximizes the scattered intensity. The curves present the photo-diode intensity at the beam center. The bold red line is a guide to the eye.

Once scattering patterns are obtained, ensuring that the particles are in the laser beam, finer scan steps along x- and z-direction determine the exact location of the interface between both particles. Thereto, the intensity at the characteristic scattering angle for crystalline PA12 is used. While scanning in the z-direction, the substrate below the particles blocks the X-ray beam whereas the air above the particles mainly results in transmission of the primary beam and small angle scattering. The photodiode intensity exhibits a weak minimum and the scattered intensity shows a weak maximum at a vertical distance between the X-ray beam and substrate that equals the particle radius, which corresponds to the desired beam location. In the x-direction, the center of the spherical particles exhibits more pronounced scattering as the thinner sides, which allows to determine the interface location as a weak minimum in scattered intensity and weak maximum in transmitted intensity. Fig. 6 shows that frame x0,z0 is the common interface location for scans along the x- and z-direction respectively. The inset graphs in Fig. 6, showing the scattering patterns and photodiode intensity values as a function of the location of the particle pair, illustrate the method.

IV. RESULTS AND DISCUSSION

To demonstrate the capabilities of the home-built laser sintering setup, as a case study, two PA12 particles with a radius of 115 μm are sintered while performing time-resolved in-situ optical imaging and X-ray characterization. The sample chamber temperature is set sufficiently below the polymer melting temperature (155 ºC versus 178 ºC). Based on the melting enthalpy of PA12, the energy to completely melt one PA12 particle is calculated to be 192 μJ. Therefore, a pulse energy of 384 μJ was applied with a pulse duration of 1 ms. As expected, raising the temperature locally at the interface above the melting temperature leads to molecular mobility which allows for fast interpenetration of polymer chains from both particles followed by viscous flow, driven by the surface tension[41]. Hence, particles sinter together and subsequently the dumbbell-shaped particle doublet undergoes a further shape relaxation, until heat loss of the material and crystallization leads to cooling and thus solidification which freezes the shape, as illustrated in Fig. 7.

To quantify the kinetics of the sintering process, the dimensionless neck radius (x/a_o) is quantified by tracking the sintering neck x, formed between the particles with initial particle radius a_o, of both particles, as defined in Fig. 7.

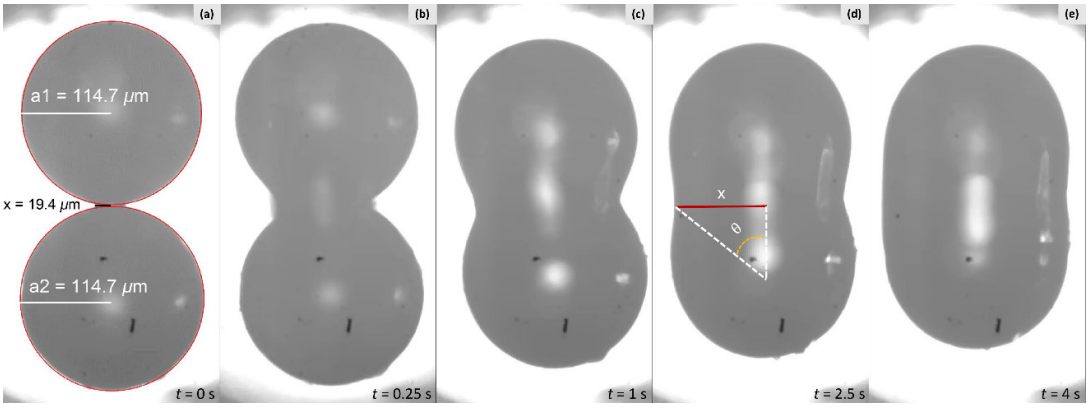

FIG. 7. Image sequence of sintering (a to e) for PA12 particle pairs of radius a_o = 115 μm, wherein heating chamber temperature T_c = 155 ºC, pulse energy E_p = 383 μJ and pulse duration t_l = 1 ms. The evolution of the neck (black line) at the interface between the two particles is followed in time.

To extract the neck and radii the image sequence was analyzed using MATLAB®. A custom-written code was used that includes the Circle Hough Transform (CHT) for finding circles and determines the distance of the neck edge to the centerline connecting both particles. Fig. 8 shows the tracked dimensionless neck plotted against sintering time. The laser is switched on at time t = 0 s and the sintering kinetics in Fig. 8 shows that the laser pulse can be considered instantaneous with respect to the sintering kinetics. The slope of the curve in Fig. 8 provides the sintering rate, and a progressive decrease in sintering rate is observed due to heat loss which eventually leads to solidification of the material[42].

Several models are available to describe isothermal viscous sintering of liquid droplets. A model for viscous sintering of two spherical equal-sized Newtonian materials was fit to the evolution of the neck, as shown in Fig. 8. The time evolution of the angle θ between the line connecting the particle centers and that connecting a particle center and the extreme point of the neck, represented in Fig. 7d, can be found from:

$$\frac{d\theta}{dt} = \frac{\Gamma}{a_o \eta} \cdot \frac{2^{-5/3} \cos\theta \sin\theta}{K_1^2 (2-\cos\theta)^{5/3} (1+\cos\theta)^{4/3}} \tag{3}$$

Where Γ denotes the surface tension, η the viscosity and a_o the particle radius. K_1 is given by[44]:

$$K_1 = \frac{\tan\theta}{2} - \frac{\sin\theta}{6} \cdot \left[\frac{2\cdot(2-\cos\theta)+(1+\cos\theta)}{(1+\cos\theta)\cdot(2-\cos\theta)}\right] \tag{4}$$

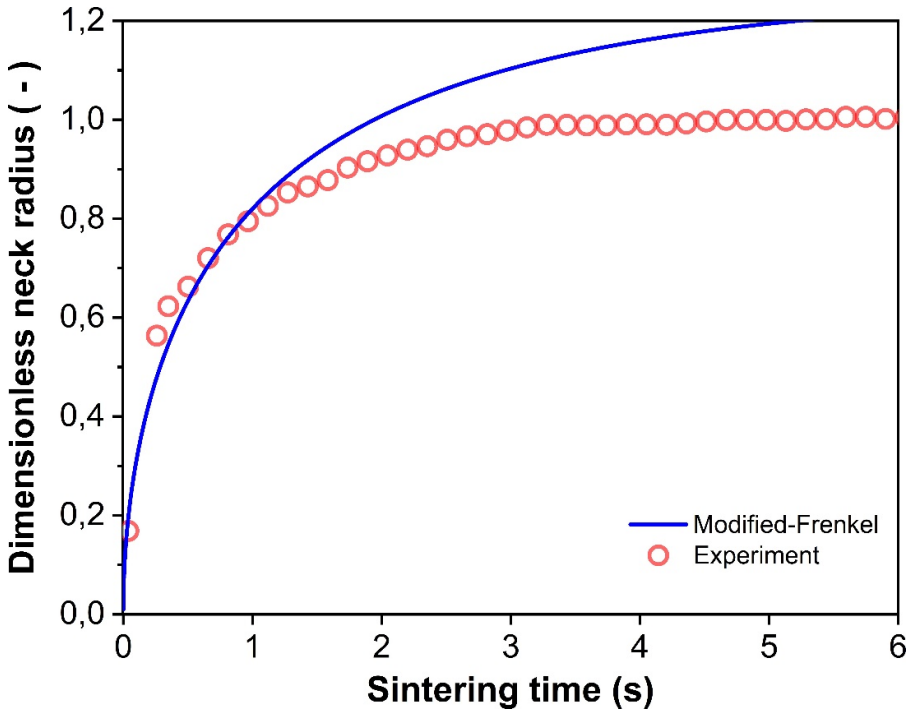

FIG. 8. Comparison of modified-Frenkel model with sintering experimental results of PA12 for a particle radius a_o = 115 μm, heating chamber temperature T_c = 155 ºC, pulse energy E_p = 383 μJ and pulse duration t_l = 1 ms. Viscosity value in the modified-Frenkel model corresponds to a constant temperature of 224 ºC.

From θ, the dimensionless neck radius x/a_o is obtained[43]:

$$\frac{x}{a_o} = \sin\theta \left(\frac{4}{(1+\sin\theta)^2 \cdot (2-\cos\theta)} \right)^{1/3} \quad (5)$$

This equation has been proven to be able to describe isothermal viscous sintering of polymer particles on a heated substrate[43]. However, in our case, isothermal conditions and a homogeneous temperature distribution across the particles are not expected due to the short laser pulse followed by cooling. Nevertheless, using a constant viscosity as a fitting parameter, the model can predict the initial sintering kinetics. The obtained viscosity value is 81 Pa·s, which according to the Arrhenius parameters for PA12, would correspond to a temperature of 224 ºC.

The subsequent cooling and solidification of the particle bridge is governed by a combination of heat diffusion from the laser illuminated area to the remainder of the particle as well as heat loss to the environment. From the heat diffusion time t in a semi-infinite medium

(t = x^2/α, with x the diffusion distance and α the thermal diffusivity) it follows that the laser heat can diffuse through the complete particle over a time of approximately 0.76 s. Heat loss to the environment mainly occurs through free convection (radiation contribution is much smaller), and will lead to a reduction of the particle temperature, according to[30]:

$$T_{\mathrm{p}}(t) = (T_{\max} - T_{\mathrm{c}}) \cdot exp\left(-\frac{hAt}{mc_{\mathrm{p}}}\right) + T_{\mathrm{c}} \quad (6)$$

where m is the mass of the particle, c_{p} the heat capacity, A the particle surface area, h the heat transfer coefficient, $T_{\max}$ the maximum temperature at the interface of the particles and T_{c} the temperature of the heating chamber. Herein, a homogeneous temperature profile throughout the particle is assumed, based on the relatively low values of the Biot number, Bi<0.6 (Bi = $h \cdot L_{\mathrm{c}}/k = h \cdot (a_{\mathrm{o}}/3)/k$, with a_{o} the particle radius, h the heat transfer coefficient, L_{c} the characteristic length and k the thermal conductivity[45]). Hence, it can be estimated that, depending on the value of h (which varies between 50 and 300 W/(m^2·K) depending on the used correlation[46]) the particles take on the order of 1.5 s to 9.8 s to cool down to 160 ºC. This timescale corresponds approximately to that of the sintering kinetics in Fig. 8. Hence, whereas with complete sintering of both particles and in the absence of pinning of the particles to the substrate, the equilibrium state would be a single nearly spherical droplet on the substrate with final droplet radius equal to $1.26a_{\mathrm{o}}$,[43] here an extended polymer shape remains after solidification. More elaborate studies combined with numerical simulations are required to fully analyze this complex process, which involves a varying and non-homogeneous temperature as well as flow profile within the particles[18].

Apart from the optical visualization of the macrostructure of the particle doublet, wide-angle X-ray diffraction experiments allow to characterize the development of the crystalline microstructure. To demonstrate how laser sintering affects the crystal morphology, the intensity profile before sintering is compared with that after sintering. Fig. 9 shows these intensity profiles, obtained from radially integrating the intensity over an azimuthal angle of 90º and plotting it versus scattering vector q for the situation before sintering and after 24 s, at which point steady state was reached. The integrated intensity, peak position, and peak width were obtained by fitting the curve with a double Gaussian-Lorentzian function[47]. To calculate crystallinity, an additional Gaussian-Lorentzian function was used to fit the amorphous background[48]. Thereto, the scattered intensity profile in the frame just before the polymer started to crystallize was used. The crystallinity was calculated from the deconvolution of the total intensity into the amorphous and crystalline contributions:

$$\chi_c = \frac{A_c}{A_c + A_a} \tag{7}$$

where χ_c is crystallinity, A_c is the area of the crystalline peaks and A_a is area of the amorphous halo.

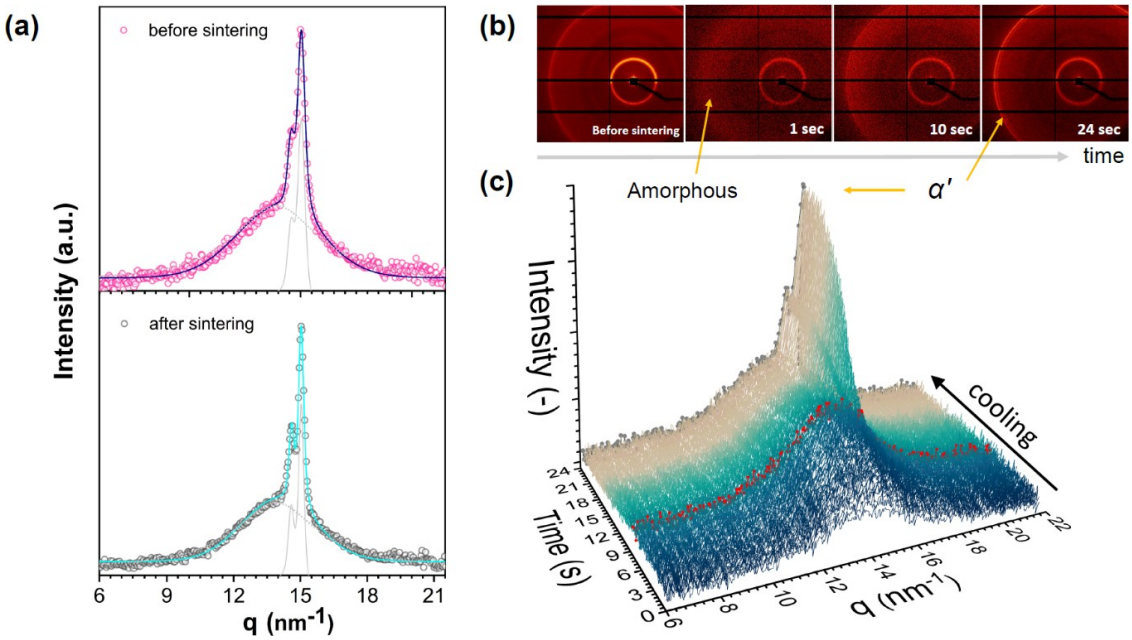

FIG. 9. (a) Integrated intensity as a function of scattering vector q, before and after sintering. The markers represent the radially integrated pattern obtained from experiments and the lines represent the sum of fitted peaks using a Gaussian-Lorentzian function. The grey dotted line is the amorphous halo and the grey solid line is the peak fit of the crystalline peak. (b) Image sequence of time-resolved 2D-WAXD patterns of PA12, before and during sintering for PA12 particles of radius a_o = 115 μm with heating chamber temperature T_c = 155 °C, pulse energy E_p = 383 μm and pulse duration t_l = 1 ms. (c) 3D plot of the radially integrated intensity as a function of scattering vector q for the complete acquisition time. Red line represents the amorphous halo before crystallization starts.

For crystallization temperatures above 130 ºC, two distinct crystalline reflections are generally visible for PA12 since above this temperature it crystallizes into a combination of γ- and α'- phase[49]. Before sintering, a distinct peak at q = 15.02 nm^{-1} (d = 0.418 nm) with a shoulder can be observed, as shown in Fig. 9 by the solid gray line. After sintering, this is transformed into two clear peaks with a secondary peak at 14.6 nm^{-1} (d = 0.430 nm). These peak positions correspond to the values given in literature for the crystalline reflections of the α'- phase in PA12, which is typical for crystallization at high temperatures[35,49]. However, some studies in literature report the opposite transition from the α' phase showing two crystalline

reflections to a γ- phase exhibiting only one reflection after sintering[50]. This phase transition is temperature sensitive and eventually forms the commonly known γ-phase when cooling down to room temperature[47,51]. Though there is a clear difference in crystal morphology, the crystallinity percentage as determined from the ratio of the integrated intensity of the crystalline peaks over the total integrated intensity, before and after sintering is about the same at around 21.3%. The crystallinity percentage can vary between 20% and 46% for PA12, depending on the grade and processing conditions[35,48,52]. Whereas previous studies are limited to the overall crystal morphology of a sintered part, our data in Fig. 9 provide the crystal details locally in the sintered particle bridge. Moreover, as local sintering parameters can be precisely controlled and flow profiles can be extracted from the growth of the neck radius[18,43], a more detailed study of the effects of processing conditions on crystallization due to sintering can be performed with our newly developed setup. Since laser sintering and corresponding flow in the neck region can lead to molecular alignment, anisotropic crystalline structures may be generated. However, under the conditions studied in the present case study, no such anisotropy of the scattering images was noticed, indicating that the flow was not strong enough to result in crystal orientation, or at least not over a substantial region of the polymer particles. It should be taken in account that the ratio of the X-ray beam diameter (100 μm) to the particle diameter (230 μm) is 0.43, whereby almost half of the particle area is irradiated, resulting in a convoluted image of the actual bridge and the neighboring region.

In addition to providing local information about the crystal structure of PA12, the second major advantage of our approach is that the time-resolved evolution of the crystallization process during sintering is available as well. Fig. 9 shows scattering patterns at different points in time after the laser pulse. Initially, during the short laser pulse, the material is molten as evidenced by the absence of the typical diffraction rings of the PA12 crystals. The typical phase transition time is of the order of 0.4 s. Over the course of time, this diffraction ring reappears indicating that the polymer starts to crystallize. The obtained intensity profiles were plotted versus the scattering vector q, at various times, as can be seen in the 3D plot in Fig. 9. This figure clearly shows that the complete phase transition from the molten amorphous state at time t = 0 s, until full solidification at t = 24 s can be followed, at the sintering zone. By determining the degree of crystallization from the diffraction patterns collected as a function of time, the crystallization kinetics can be analyzed, as shown in Fig. 10. Crystallinity is absent at the instant the laser pulse hits the interface of the particles, at time t = 0 s. The onset of solidification from the molten amorphous to the solid semi-crystalline state can be observed at time t = 8 s as the particles undergo cooling until crystallization ends at time t = 24 s. The half-

time of the crystallization, as obtained from Fig. 10, is 13 s. As mentioned before in section III(A), under isothermal and quiescent conditions, $t_{1/2}$is about 19.5 s at 155 °C and it has been shown that this time increases with temperature up to the melt temperature[35]. Since the temperature during laser sintering evolves from a relatively high temperature directly after the laser pulse to minimum 155 ºC, it is clear that the observed crystallization kinetics is faster than expected from the quiescent crystallization kinetics. This could be due to the flow originating from the bridge growth process, demonstrated in Fig. 8, which can affect the crystallization process. Similar increases in crystallization kinetics due to flow have been observed for many polymers[53]. However, for PA12 the flow-induced crystallization kinetics has not yet been systematically analyzed. Therefore, quantitative comparison of the crystallization kinetics observed here with that under standard flow conditions is not possible. Finally, by comparing the kinetics in Figs. 8 and 10, it can be seen that under the studied conditions, the macrostructural kinetics in the form of the neck growth has a much faster timescale as compared to the crystallization. By tuning the laser energy, pulse duration and chamber temperature, it will be possible to alter both timescales independently as the first one mainly depends upon the polymer viscosity whereas the second depends on a combination of shear and temperature effects. Hence, a wealth of possible processing conditions can be generated, possibly resulting in a variety of crystalline microstructures.

These preliminary data from a case study on PA12 particles demonstrate the unique capability of our setup to capture the kinetics of the development of the macrostructure in the form of neck-radius growth as well as the microstructure in the form of crystallinity and crystal-type evolution during laser sintering. The results also illustrate the accuracy with which these features can be obtained. Hence, future experiments at different processing conditions will provide us with critical information about the laser sintering process. In addition, different classes of polymers ranging from commodity polymers like polystyrene to high performance polymers like polyether ether ketone can be sintered in the setup. The setup is also flexible towards the use of small angle X-ray scattering or more local characterizations using a more pronounced focusing of the X-ray beam.

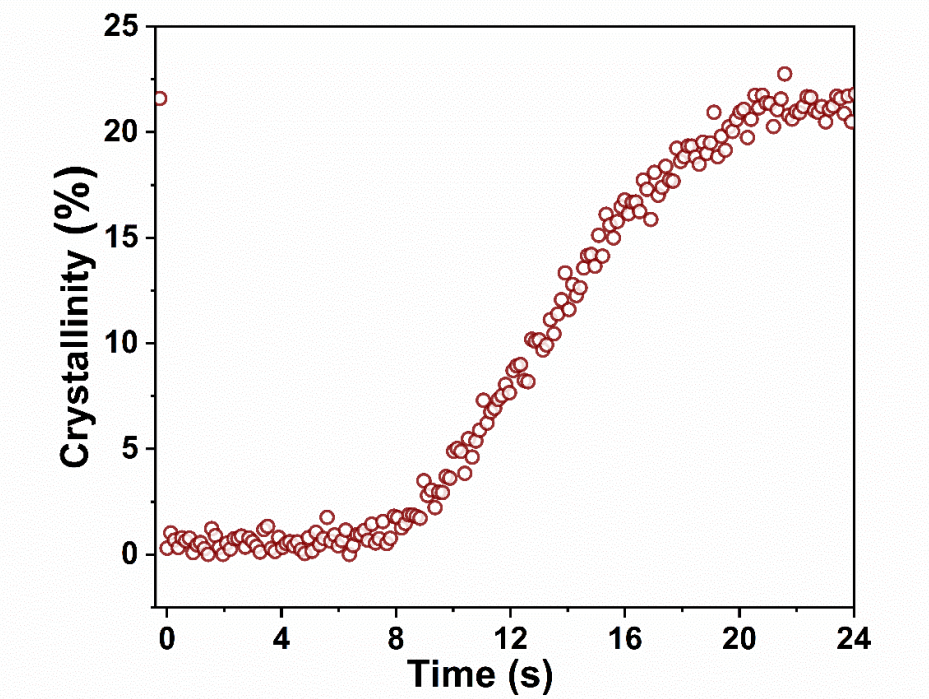

FIG. 10. Time evolution of crystallinity during the sintering process for PA12 particles of radius a_o = 115 μm, heating chamber temperature T_c = 155 ºC, pulse energy E_p = 383 μm and pulse duration t_l = 1 ms.

V. CONCLUSIONS

A novel in-house developed experimental laser sintering setup has been designed and constructed that has the unique ability to allow in-situ time-resolved microscopic and X-ray observations of laser sintering with precise control over all sintering parameters. A case study on the sintering of PA12 particle pairs demonstrates that real-time information about the sintering dynamics as well as crystallization kinetics can be obtained with a good signal-to-noise ratio and with sufficient spatial and temporal resolution. Since structure evolution and crystallization kinetics during laser sintering are complex and coupled processes involving non-isothermal, non-homogeneous temperature profiles and complex flow fields, this laser sintering setup provides direct access to essential local and time-resolved information about the structural processes involved. Future experiments using this setup can provide us with essential knowledge to understand the relations between sintering conditions and microstructure development. Hence, the unique device opens up new promising perspectives in the field of 3D printing by selective laser sintering.

ACKNOWLEDGMENTS

This work forms part of the research programme of the Brightlands Materials Center (BMC). We acknowledge the European Synchrotron Radiation Facility (ESRF) for provision of synchrotron radiation facilities and NWO for financing beam time at ESRF. We would like to thank Dr. Daniel Hermida Merino for assistance in using the Dutch-Belgian beamline (DUBBLE) BM26 and Prof. Dr. ir. Leon E. Govaert for providing the PA12 polymer. We also thank Dr. Rob Satnik from Acal BFi for supplying components and helpful discussion on laser alignment.

REFERENCES

[1]C. R. Deckard, US Patent **4**, 863 (1989).

[2]J. P. Kruth, T. L. X. Wang, and L. Froyen, Assembly Automation **23(4)**, 357 (2003).

[3]K. H. Tan, C. K. Chua, K. F. Leong, C. M. Cheah, W. S. Gui, W. S. Tan, and F. E. Wiria, Bio-medical Materials and Engineering **15(1,2)**, 113 (2005).

[4]S. Kumar, JOM **55(10)**, 43 (2003).

[5]E. Radstok, Rapid tooling, Rapid Prototyping Journal **5(4)**, 164 (1999).

[6]M. Schmid, A. Amado, and K. Wegener, Journal of Materials Research **29**, 1824 (2014).

[7]E. MacDonald and R. Wicker, Science **353(6307)**, 2093 (2016).

[8]F. S. Fogliatto, S. Flavio, and G. J. C. D. Silveira, *Mass customization: engineering and managing global operations* (Springer Science, 2010).

[9]I. Gibson, D. W. Rosen, and B. Stucker, *Design for additive manufacturing* (Springer, 2010).

[10]N. Hopkinson, C. E. Majewski, and H. Zarringhalam, CIRP annals **58 (1)**, 197 (2009).

[11]R. D. Goodridge, C. J. Tuck, and R. J. M. Hague, Progress in Materials Science **57**, 229 (2012).

[12]H. Zarringhalam, C. Majewski, and N. Hopkinson, Rapid Prototyping Journal **15**, 126 (2009).

[13]E. Moeskops, N. Kamperman, B. van de Vorst, and R. Knopppers, Proceedings of SFF, Austin USA (2004).

[14]M. Vasquez, B. Haworth, and N. Hopkinson, Polymer Engineering & Science **53**, 1230 (2013).

[15]C. T. Bellehumeur, M. K. Bisaria, and J. Vlachopoulos, Polymer Engineering & Science **36**, 2198 (1996).

[16]C. T. Bellehumeur, M. Kontopoulou, and J. Vlachopoulos, Rheologica acta **37**, 270 (1998).
[17]S. Aid, A. Eddhahak, Z. Ortega, D. Froelich, and A. Tcharkhtchi, Journal of Materials Science **52**, 11725 (2017).
[18]C. Balemans, N. O. Jaensson, M. A. Hulsen, and P. D. Anderson, Additive Manufacturing **24**, 528 (2018).
[19]I. Gibson and D. Shi, Rapid Prototyping Journal **3**, 129 (1997).
[20]R. J. Roe et. al., *Methods of X-ray and neutron scattering in polymer science* (Oxford University Press on Demand, 2000).
[21]W. Zhu, C. Yan, Y. Shi, S. Wen, J. Liu, and Y. Shi, Materials and Design **82**, 37 (2015).
[22]J. Chang, Z. Wang, X. Tang, F. Tian, K. Ye, and L. Li, Review of Scientific Instruments **89**, 025101 (2018).
[23]S. Rendon, J. Fang, W. R. Burghardt, and R. A. Bubeck, Review of Scientific Instruments **80**, 043902 (2009).
[24]E. Troisi, M. van Drongelen, H. Caelers, G. Portale, and G. Peters, European Polymer Journal **74**, 190 (2016).
[25]J. E. Seppala and K. D. Migler, Additive manufacturing **12**, 71 (2016).
[26]L. A. Northcutt, S. V. Orski, K. B. Migler, and A. P. Kotula, Polymer **154**, 182 (2018).
[27]C. L. A. Leung, S. Marussi, R. C. Atwood, M. Towrie, P. J. Withers, and P. D. Lee, Nature Communications **9**, 1355 (2018).
[28]Q. Guo, C. Zhao, L. I. Escano, Z. Young, L. Xiong, K. Fezzaa, W. Everhart, B. Brown, T. Sun, and L. Chen, Acta Materialia **151**, 169 (2018).
[29]C. Zhao, K. Fezzaa, R. W. Cunningham, H. Wen, F. De Carlo, L. Chen, A. D. Rollett, and T. Sun, Scientific Reports **7**, 3602 (2017).
[30]P. Hejmady, L. C. A. van Breemen, P. D. Anderson, and R. Cardinaels, Soft Matter **15**, 1373 (2019).
[31]W. M. Steen and J. Mazumder, *Laser material processing* (Springer Science & Business Media, 2010).
[32]G. Portale, D. Cavallo, G. C. Alfonso, D. Hermida-Merino, M. van Drongelen, L. Balzano, G. W. M. Peters, J. G. P. Goossens, and W. Bras, Journal of Applied Crystallography **46(6)**, 1681 (2013).
[33]A. P. Hammersley and et. al., European Synchrotron Radiation Facility Internal Report **68**, 58 (1997).
[34]R. Androsch, M. L. Di Lorenzo, and C. Schick, European Polymer Journal **96**, 361 (2017).

667 [35]F. Paolucci, P. C. R. D. Baeten, B. Goderis, and G. W. M. Peters, Polymer **155**, 187 (2018).
668 [36]C. Y. Liu, J. He, R. Keunings, and C. Bailly, Macromolecules **39**(25), 8867 (2006).
669 [37]L. Verbelen, S. Dadbakhsh, M. Van den Eynde, J. P. Kruth, B. Goderis, and P. Van Puyvelde,
670 European Polymer Journal **75**, 163 (2016).
671 [38]B. B. Sauer and G. T. Dee, Macromolecules **35(18)**, 7024 (2002).
672 [39]M. Yuan, T. Diller, Timothy, D. Bourell, and J. Beaman, Rapid Prototyping Journal **19(6)**,
673 437 (2013).
674 [40]H. Kawamoto and K. Tsuji, Advanced Powder Technology **22**, 602 (2011).
675 [41]M. Wu, T. Cubaud, and C. M. Ho, Physics of Fluids **16**, L51 (2004).
676 [42]A. J. Shaler, JOM **1**, 796 (1949).
677 [43]O. Pokluda, C. T. Bellehumeur, and J. Vlachopoulos, AIChE journal **43**, 3253 (1997).
678 [44]E. Scribben, D. Baird, and P. Wapperom, Rheologica acta **45**, 825 (2006).
679 [45]W. M. Rohsenow, J. P. Hartnett, and Y. I. Cho, *Handbook of heat transfer*, Vol. 3 (1998).
680 [46]F. P. Incropera, A. S. Lavine, T. L. Bergman, and D. P. DeWitt, *Fundamentals of heat and*
681 *mass transfer* (Wiley, 2007).
682 [47]L. Li, M. H. J. Koch, and W. H. de Jeu, Macromolecules **36**, 1626 (2003).
683 [48]N. Dencheva, T. G. Nunes, M. J. Oliveira, and Z. Denchev, Journal of Polymer Science Part
684 B: Polymer Physics **43**, 3720 (2005).
685 [49]C. Ramesh, Macromolecules **32**, 5704 (1999).
686 [50]S. Dadbakhsh, L. Verbelen, O. Verkinderen, D. Strobbe, P. V. Puyvelde, and J. P. Kruth,
687 European Polymer Journal **92**, 250 (2017).
688 [51]N. Hiramatsu, K. Haraguchi, and H. Susumu, Japanese Journal of Applied Physics **22**, 335
689 (1983).
690 [52]S. Dupin, O. Lame, C. Barrès, and J.-Y. Charmeau, European Polymer Journal **48**, 1611
691 (2012).
692 [53]E. M. Troisi, H. J. M. Caelers, and G. W. M. Peters, Macromolecules **50(10)**, 3868 (2017).

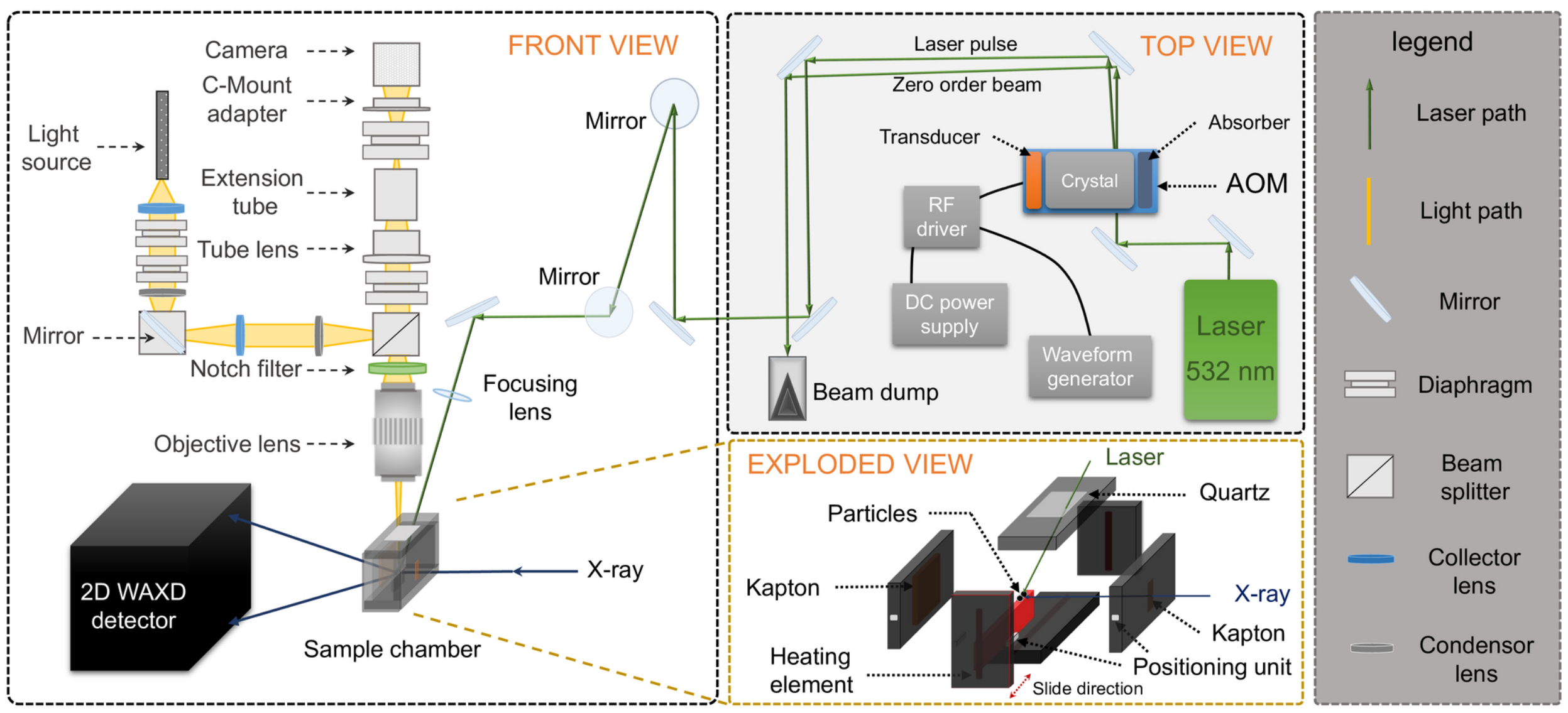
FRONT VIEW
Camera
C-Mount adapter
Light source
Extension tube
Tube lens
Mirror
Notch filter
Objective lens
Mirror
Mirror
Focusing lens
2D WAXD detector
X-ray
Sample chamber
TOP VIEW
Laser pulse
Zero order beam
Transducer
Absorber
Crystal
AOM
RF driver
DC power supply
Waveform generator
Laser 532 nm
Beam dump
EXPLODED VIEW
Laser
Quartz
Particles
Kapton
X-ray
Kapton
Heating element
Positioning unit
Slide direction
legend
Laser path
Light path
Mirror
Diaphragm
Beam splitter
Collector lens
Condensor lens

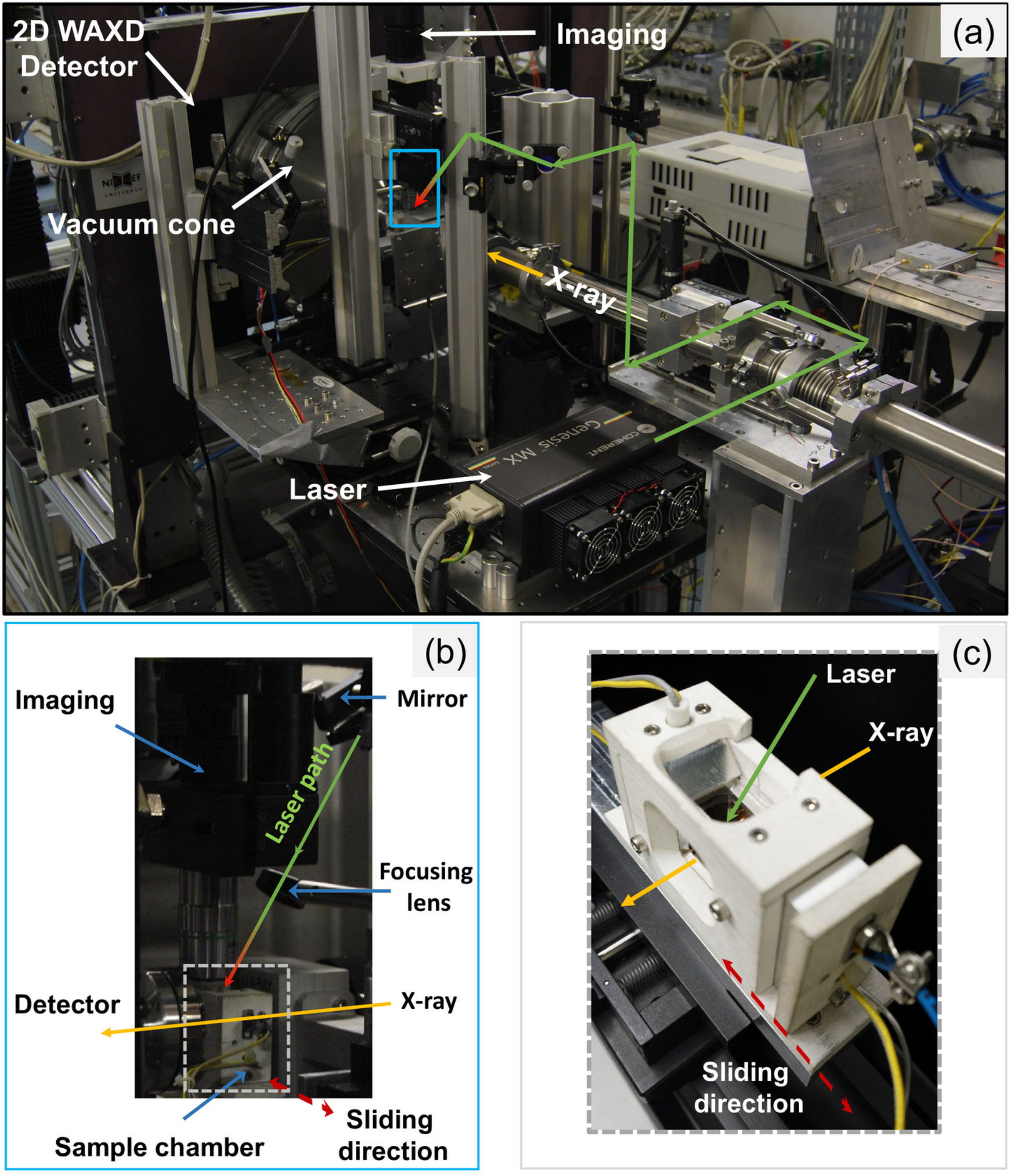
(a)
2D WAXD Detector
Imaging
Vacuum cone
X-ray
Laser
(b)
Imaging
Mirror
Laser path
Focusing lens
Detector
X-ray
Sample chamber
Sliding direction
(c)
Laser
X-ray
Sliding direction

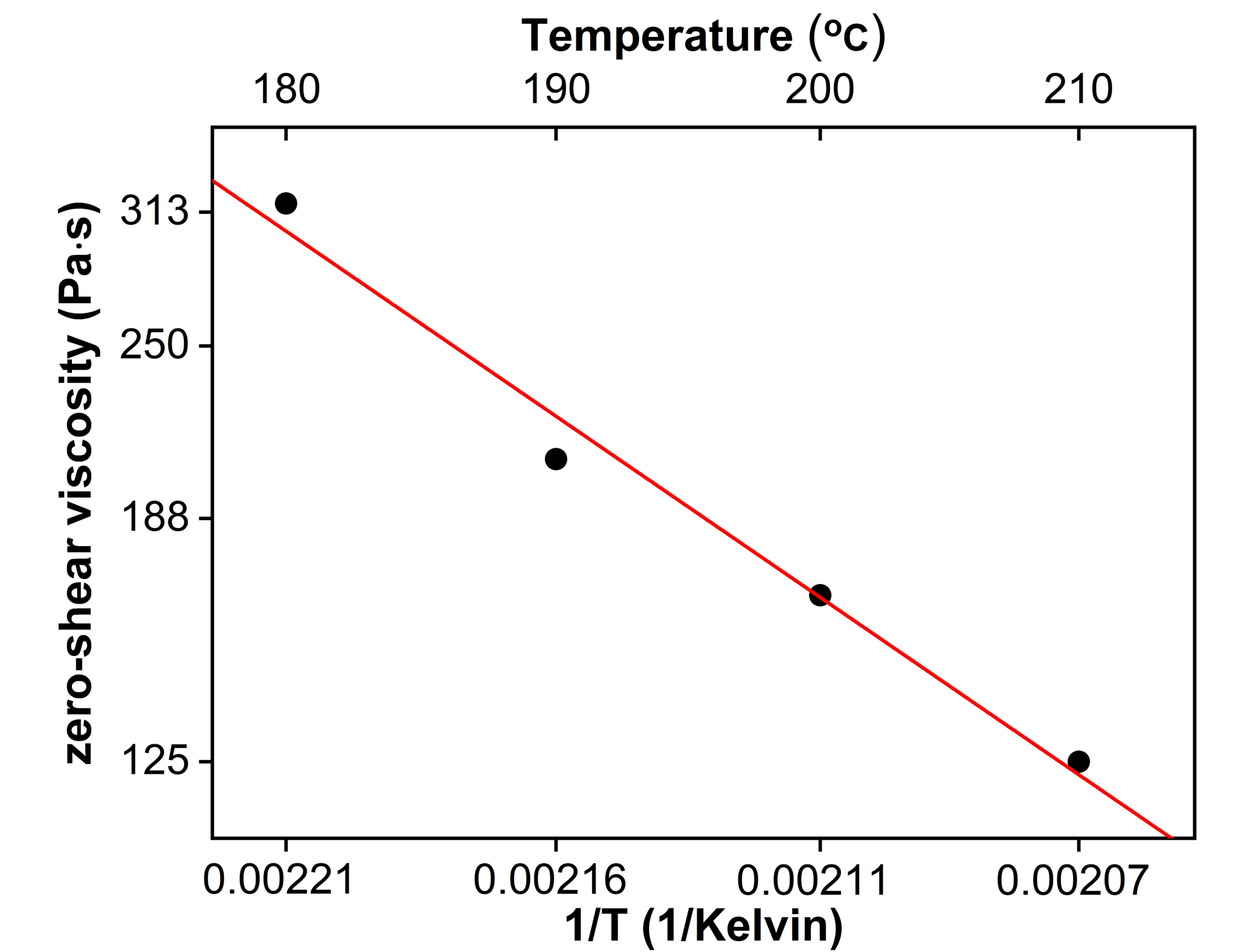
Temperature (°C)
180
190
200
210
zero-shear viscosity (Pa·s)
313
250
188
125
0.00221
0.00216
0.00211
0.00207
1/T (1/Kelvin)

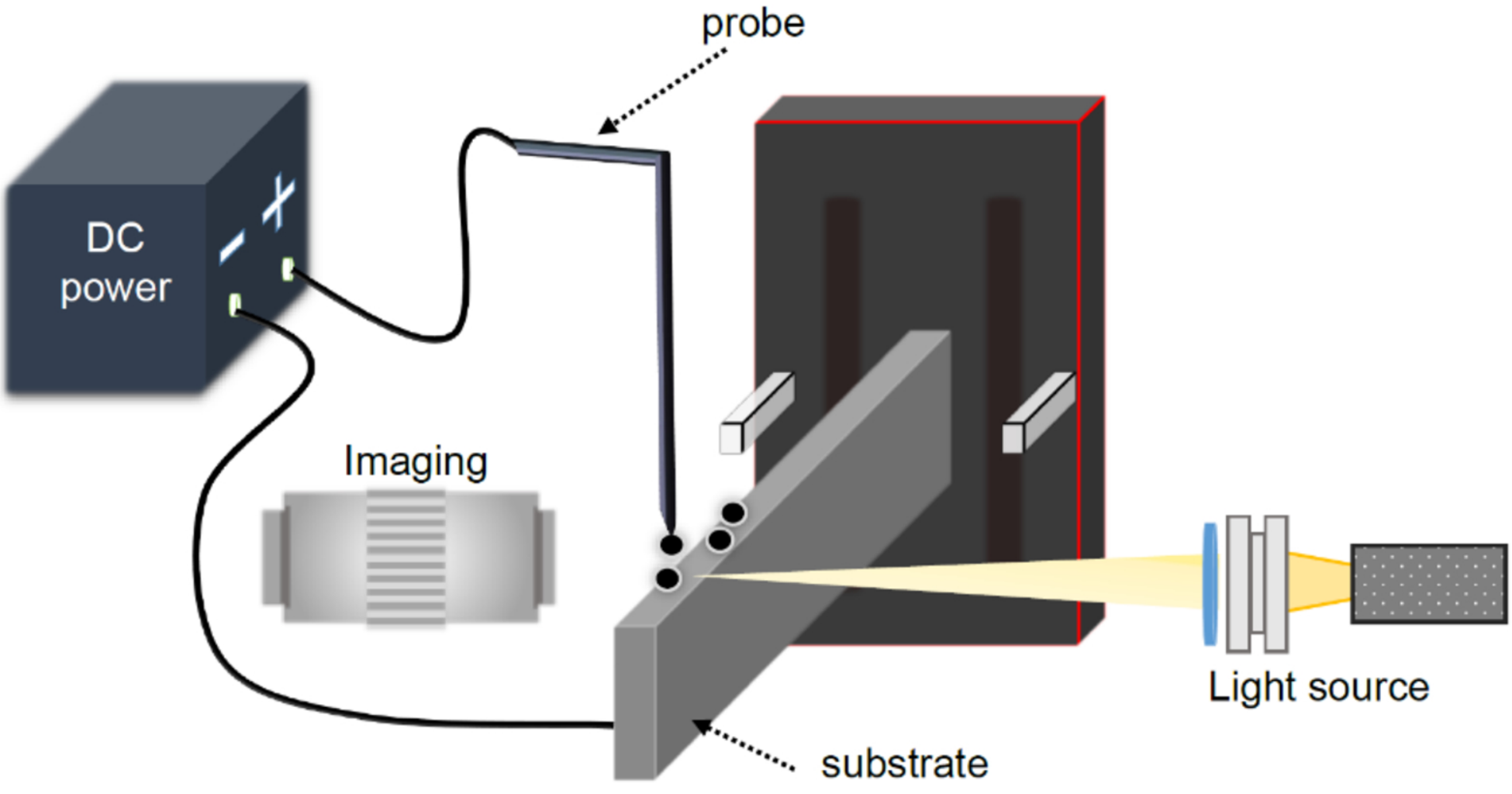
probe
DC
power
Imaging
Light source
substrate

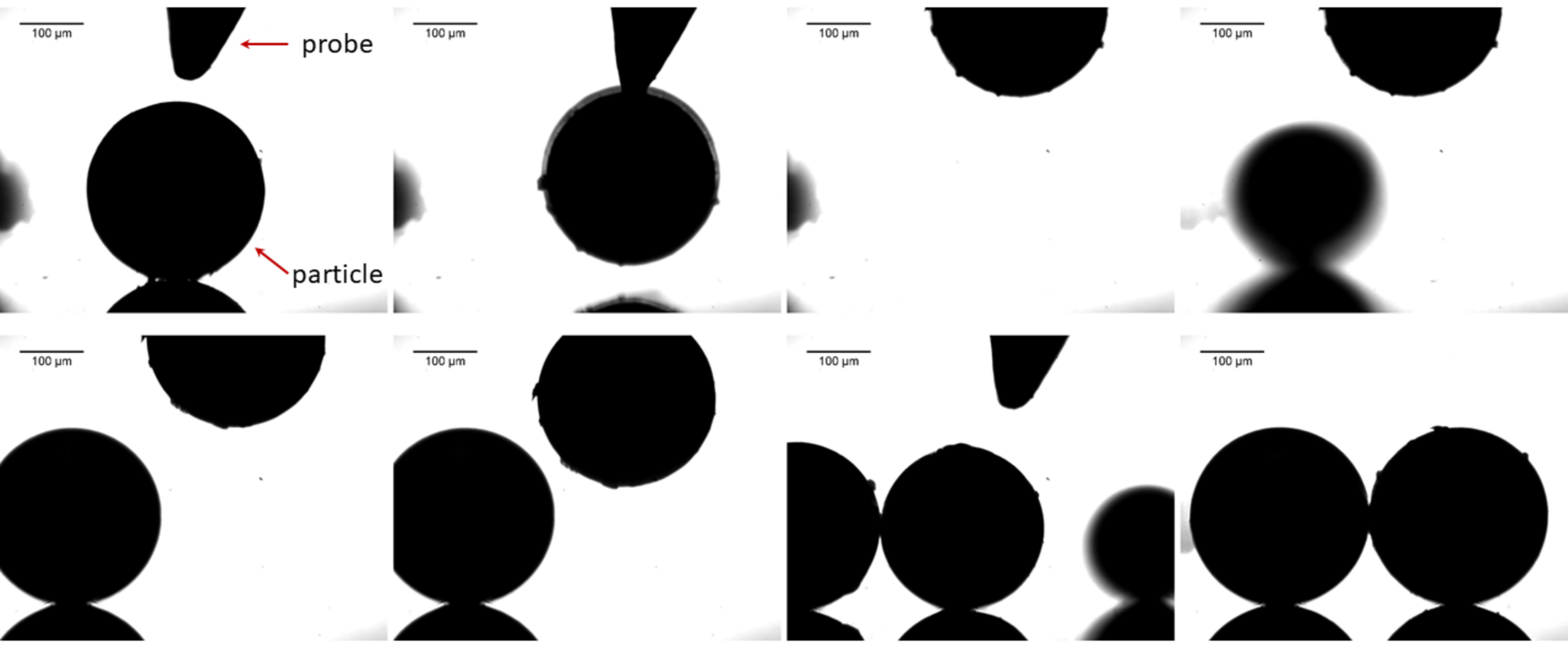
100 µm
probe
particle
100 µm
100 µm
100 µm
100 µm
100 µm
100 µm
100 µm

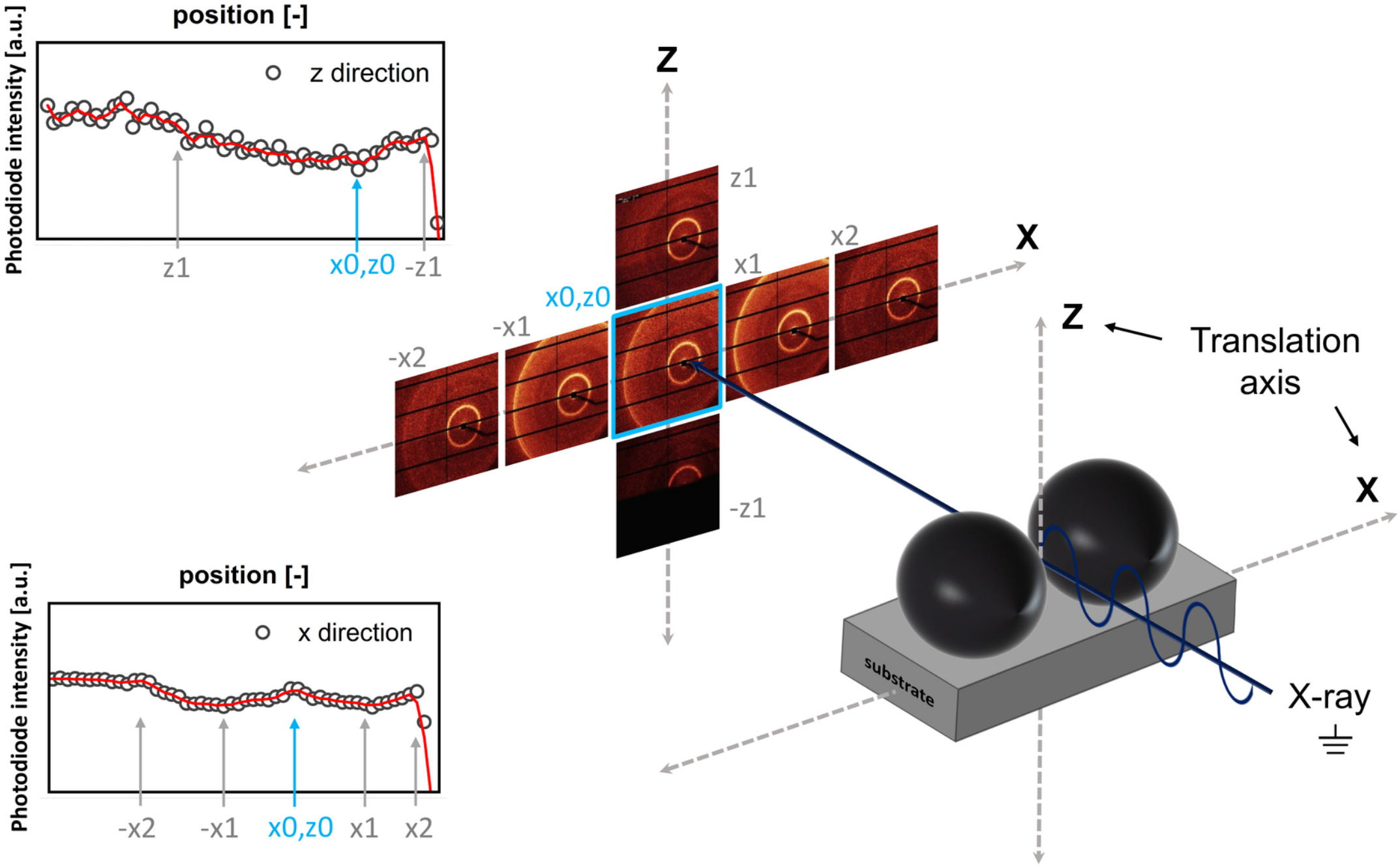
position [-]
Photodiode intensity [a.u.]
z direction
z1
x0,z0
-z1
Z
X
z1
x1
x2
x0,z0
-x1
-x2
-z1
Z
Translation
axis
X
substrate
X-ray
position [-]
Photodiode intensity [a.u.]
x direction
-x2
-x1
x0,z0
x1
x2

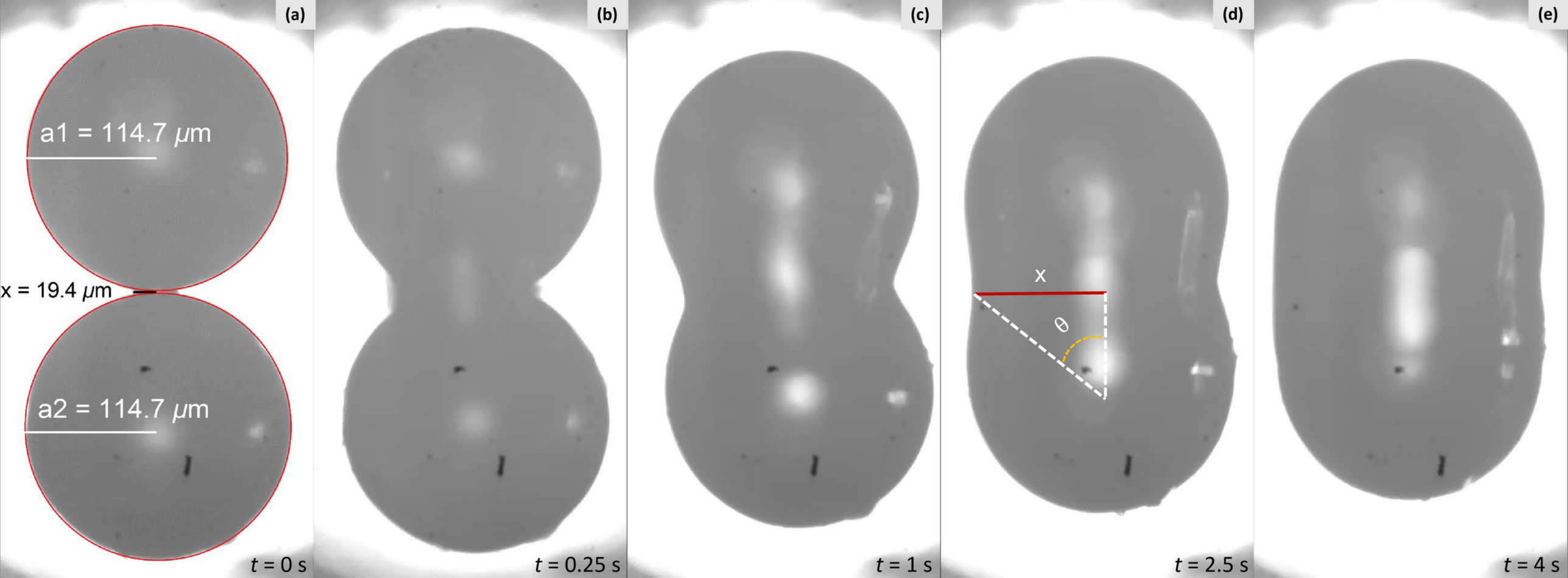
(a)
a1 = 114.7 μm
x = 19.4 μm
a2 = 114.7 μm
t = 0 s
(b)
t = 0.25 s
(c)
t = 1 s
(d)
x
Θ
t = 2.5 s
(e)
t = 4 s

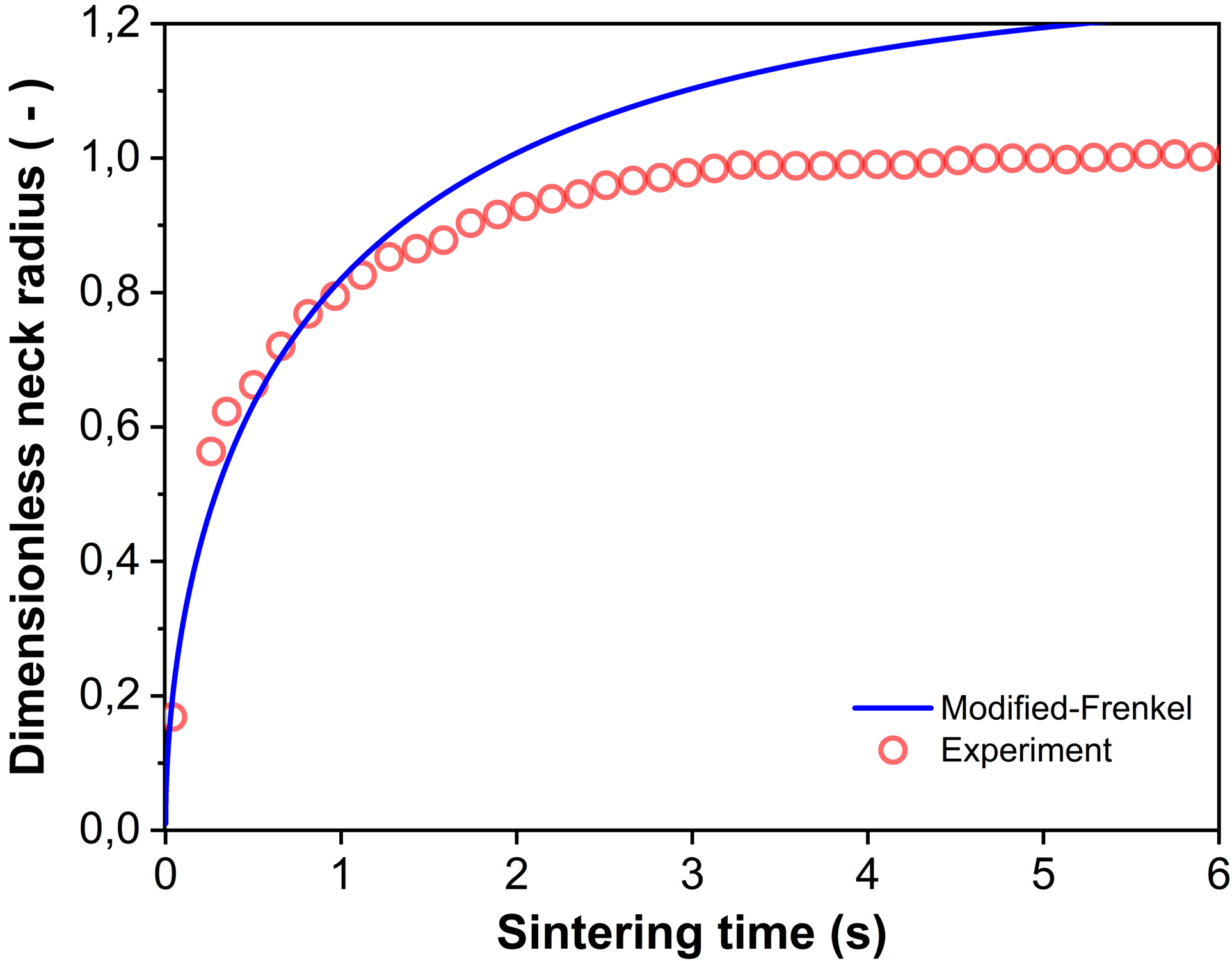
Dimensionless neck radius (-)
1,2
1,0
0,8
0,6
0,4
0,2
0,0
0
1
2
3
4
5
6
Sintering time (s)
Modified-Frenkel
Experiment

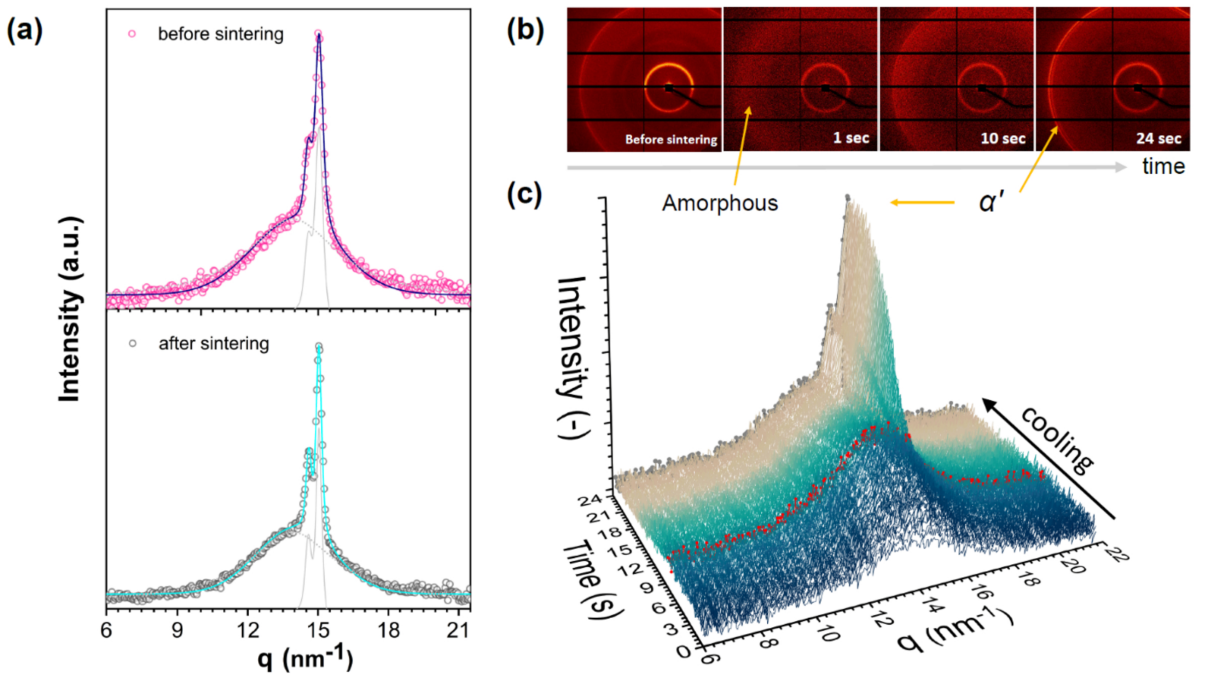
(a)
before sintering
after sintering
Intensity (a.u.)
6
9
12
15
18
21
q (nm-1)
(b)
Before sintering
1 sec
10 sec
24 sec
time
(c)
Amorphous
α′
Intensity (-)
cooling
Time (s)
q (nm-1)

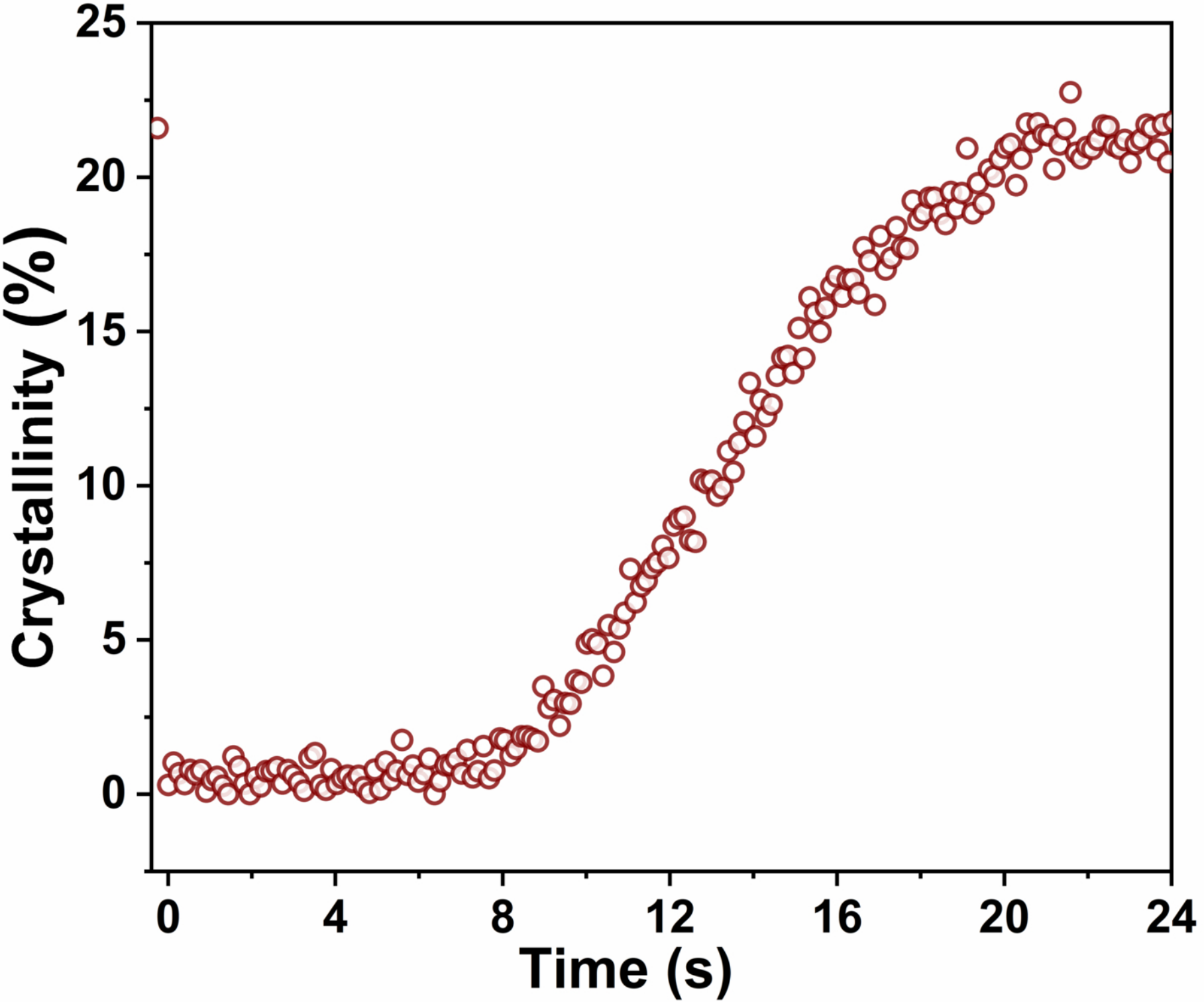
Crystallinity (%)
25
20
15
10
5
0
0
4
8
12
16
20
24
Time (s)